Drying dynamics of sessile-droplet arrays

Azmaine Iqtidar,[1,*] Joseph J. Kilbride,[2,*] Fouzia F. Ouali,[2]
David J. Fairhurst,[2] Howard A. Stone,[1,†] and Hassan Masoud[3,‡]

[1] *Department of Mechanical and Aerospace Engineering, Princeton University, Princeton, New Jersey 08544, USA*
[2] *Department of Physics and Mathematics, Nottingham Trent University, Clifton Lane, Nottingham NG11 8NS, UK*
[3] *Department of Mechanical Engineering-Engineering Mechanics, Michigan Technological University, Houghton, Michigan 49931, USA*

(Dated: January 17, 2023)

We analyze the diffusion-controlled evaporation of multiple droplets placed near each other on a planar substrate. Specifically, we calculate the change in the volume of sessile droplets with various initial contact angles that are arranged in different configurations. The calculations are supplemented by experimental measurements using a technique that interprets the variable magnification of a pattern placed beneath the droplet array, which is applied to the case of initially hemispherical droplets deposited in four distinct arrangements. We find excellent agreement between the predictions based on the theory of Masoud et al. [Evaporation of multiple droplets, J. Fluid Mech. 927, R4 (2021)] and the data gathered experimentally. Perhaps unexpectedly, we also find that, when comparing different arrays, the droplets with the same order of disappearance within their respective array, i.e., fastest evaporating, second-fastest evaporating, etc., follow similar drying dynamics. Our study provides not only experimental validation of the theoretical framework introduced by Masoud et al., but also offers additional insights into the evolution of the volume of individual droplets when evaporating within closely-spaced arrays.

I. INTRODUCTION

Diffusion-controlled evaporation of sessile droplets is a common occurrence in everyday life, as well as in a myriad of technologically advanced applications [1–3]. The ubiquity and significance of this phenomenon have motivated researchers from different fields to examine it in detail. In particular, the last two decades have witnessed a surge in the number of studies centered on the evaporation of sessile droplets and the phenomena taking place as a result or concurrent with it. A comprehensive list of books and review articles that highlight major contributions to this subject can be found in Ref. [3]. Among recent investigations, the theoretical development of Masoud *et al.* [4] (see also [5]) extended the predictive power of the diffusion-limited model for the evaporation of a single droplet to a broad range of conditions involving multiple drops. The framework is based on Green's second identity and the method of reflections, so the extended model is not restricted to thin droplets, i.e., those with small contact angles, which is the limitation of Fabrikant's model [6] utilized in the work of Wray *et al.* [7]. The approach of Masoud *et al.* [4], in fact, allows for arbitrary configurations of multiple droplets of different sizes and different, but arbitrary, contact angles. In the framework of this approach, the determination of the mass flux from each drop in the array only requires solving a linear system of equations, with the prediction errors shown to be small (within a few percent) for a wide range of multiple-droplet configurations.

Here we use the theory of Masoud *et al.* [4] to examine the collective drying of multiple sessile droplets in arrays of various configurations. In particular, we track the variations of the volume of individual droplets over time while evaporating under constant radius (CR) or constant contact angle (CA) conditions. We consider droplets of different initial contact angles, ranging from $\pi/3$ to $2\pi/3$. Our theoretical calculations are accompanied by a set of experiments, where the change in the volume of evaporating droplets was measured from the magnification of a pattern of dots placed underneath them. The initial contact angles of the drops in the experiments were about $\pi/2$ and their contact radii (about 1 mm) remained pinned during most of their lifetimes. Furthermore, in the experiments, the droplets were placed in four different configurations, namely triangle (vertices), cross, pentagon (vertices and middle), and a 3×3 grid, where in each configuration the center-to-center distance between the nearest droplets was roughly three times their contact radius.

The outcome of our combined theoretical and experimental investigation is twofold. First, we show very close agreement between the theoretical predictions and experimental measurements, which further validates the fidelity

* Authors of equal contribution
† hastone@princeton.edu
‡ hmasoud@mtu.edu

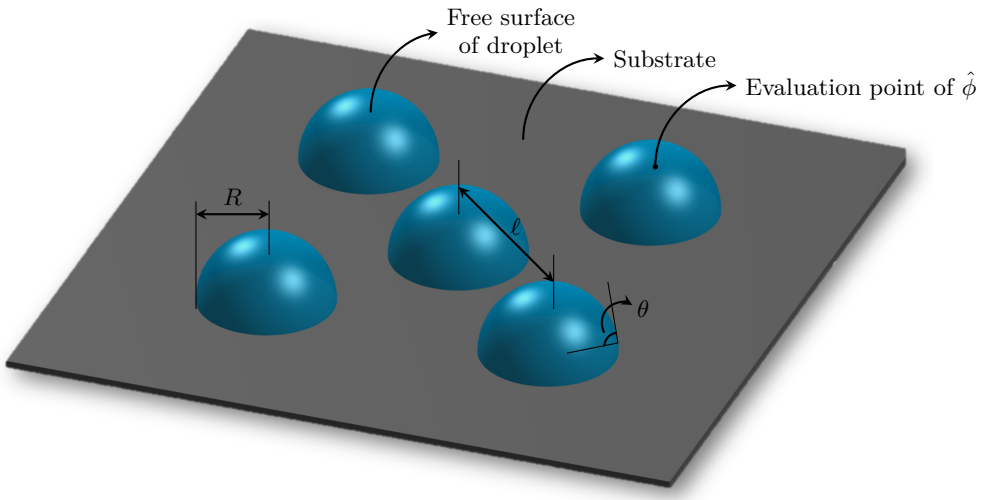

FIG. 1: Schematic of an array of evaporating sessile droplets.

of the theoretical model. Second, we present data indicating that the drying dynamics of droplets within an array is heavily dependent on their order of disappearance, i.e., the fastest evaporating or second-fastest evaporating, etc., rather than the specific arrangement of the droplets. This behavior, we believe, has not been reported elsewhere. Overall, our findings shed additional light on the collective effects at play during the drying of sessile-droplet arrays, and, by doing so, complement the existing body of literature on the topic. Below, we first explain our methodology, beginning with the description of the theoretical approach followed by the details of the experimental procedure (§ II). The results are presented and discussed in § III and concluding remarks are given in § IV.

II. METHODS

A. Theoretical Approach

Consider a collection of droplets (numbered $n = 1, 2, \cdots, N$) evaporating purely under the influence of diffusion due to the difference in the vapor concentration on their free surface (denoted c_s) and in the far-field (denoted c_∞) (see Fig. 1). In this situation, the distribution of the vapor concentration field (denoted c) is governed by the Laplace equation and, hence, the evaporation rate of each droplet determines, and is determined by, how fast the neighboring droplets evaporate. It is convenient to denote $\hat{J}_n$ and $\hat{c}$, respectively, as the total rate of evaporation and dimensional concentration field for an isolated drop on the plane, and to denote J_n as the instantaneous total rate of mass loss from the n-th droplet in an array of drops. Masoud *et al.* [4] derived an approximate system of equations for J_n in the form of

$$\hat{J}_n \approx J_n + \sum_{\substack{m=1,\\ m\neq n}}^{N} \hat{\phi}\Big|_{r=r_m} J_m. \tag{1}$$

The function $\hat{\phi} = (\hat{c} - c_s)\,/\,(c_s - c_\infty)$ in the above equation, evaluated at the position $\boldsymbol{r} = \boldsymbol{r}_m$, represents the dimensionless concentration field corresponding to the evaporation of the n-th droplet in the absence of other drops. This field is known and can be calculated exactly [8, 9] or approximately [4] for spherical-cap droplets. Also, the evaluation point $\boldsymbol{r}_m$ is set to be the geometric center of the free surface of the m-th droplet (see Fig. 1). The approximation error of Eq. (1) was shown to be generally small for a broad range of droplet arrangements, with more accurate predictions expected for configurations with larger inter-particle distances and thinner droplets. Also, within an array, the lowest and highest errors typically correspond to the least and most confined droplets, respectively. For instance, when compared with the results of direct numerical simulations, the prediction errors for initially hemispherical droplets placed in triangle, cross, pentagon, and square patterns (see Fig. 2) did not exceed 1%, 3%, 8%, and 12%, respectively, for $\ell = 3R$, where ℓ represents the minimum center-to-center distance between droplet pairs and R is the droplets' base radius (see Fig. 1).

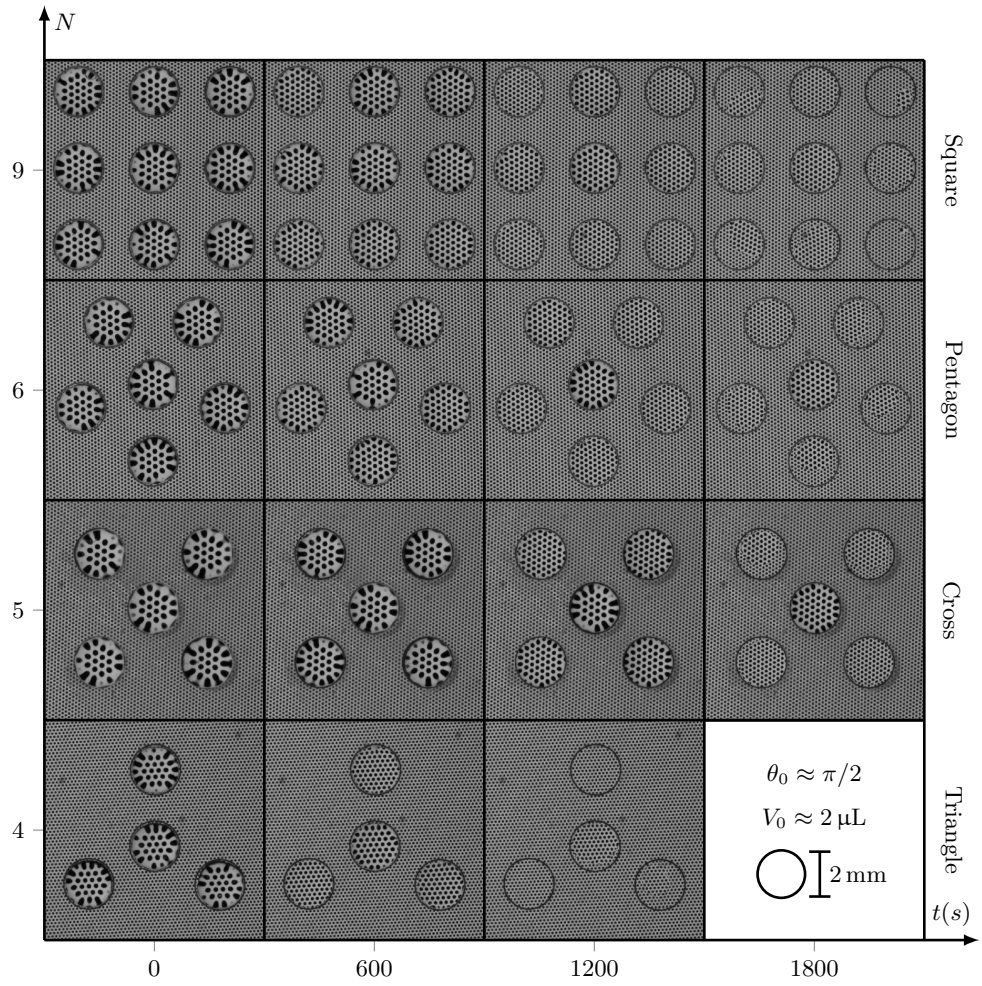

FIG. 2: Experimental images of droplet arrays magnifying a pattern of dots (ordered vertically by the number of droplets N) as a function of time for the triangle, cross, pentagon, and square configurations, corresponding to subfigures g, j, l, and m of Fig. 7 (in appendix), respectively. The legend indicates the droplets' scale, initial ($t = 0$) contact angle θ_0, and volume V_0. The minimum center-to-center distance between the nearest droplets in each configuration is about three times their contact radius.

The instantaneous evaporation rates calculated from Eq. (1) determine the time rate of change in the volume of the droplets via

$$J_n = \rho\, dV_n/dt, \tag{2}$$

where ρ and V_n denote the density and volume of the droplets, respectively. We integrated Eq. (2) in time using the Euler scheme. Consistent with the diffusion-dominated limit in which Eq. (1) was derived, at each time step, the coefficients of the linear system for J_n, i.e., $\hat{J}_n$ and $\hat{\phi}|_{r=r_m}$, were determined by the shape of the drops at that time instant. Also, we assumed that all drops have the same constant density and that they maintained spherical-cap shapes, with their volume shrinking as a result of either a decrease in their contact angle (CR mode) or contact radius (CA mode). This feature allowed us to specify the geometry of the droplets at every time instant, given their volume.

B. Experimental approach

Tracking the volume of an evaporating sessile droplet in isolation or multiple droplets arranged in a line can be accomplished with conventional side-view imaging techniques. However, this approach is not as effective for tight two-dimensional arrangements because some droplets will be obstructed or out of focus. Indeed, top-view interferometric imaging was successfully utilized by Edwards *et al.* [10] to simultaneously measure the change in heights of evaporating

sessile-droplet arrays. Here, we employ a new simpler lensing technique to determine each droplet's absolute volume. To do this, a pattern of dots is placed beneath the droplet array and imaged from above, to monitor its distortion during evaporation. Under CR mode, the radius of curvature of an evaporating droplet increases over time (provided the initial contact angle is less than $\pi/2$), which results in a decrease in the magnification of the distorted dot pattern. To relate this to the droplet height h, each droplet is treated as a plano-convex lens with an upper surface assumed spherical due to the Bond number being small (see, for example, [11]), i.e., $\mathrm{Bo} = \Delta\rho g h^2/\sigma \ll 1$, where $\Delta\rho$ is the density difference between the water and air, g is the gravitational acceleration, and σ is the water surface tension. An optics transfer matrix method is used to trace a ray of light from the pattern through the substrate, droplet, and air, and to derive an equation relating the magnification of the distorted dots to height. By solving this equation for h and knowing the base radius, the drop volume is calculated. The derivation of this pattern distortion equation will be detailed in a forthcoming article [12].

In our experiments, 2.00 ± 0.25 µL droplets of de-ionised water (PURELAB Chorus 1 – ELGA) with surface tension

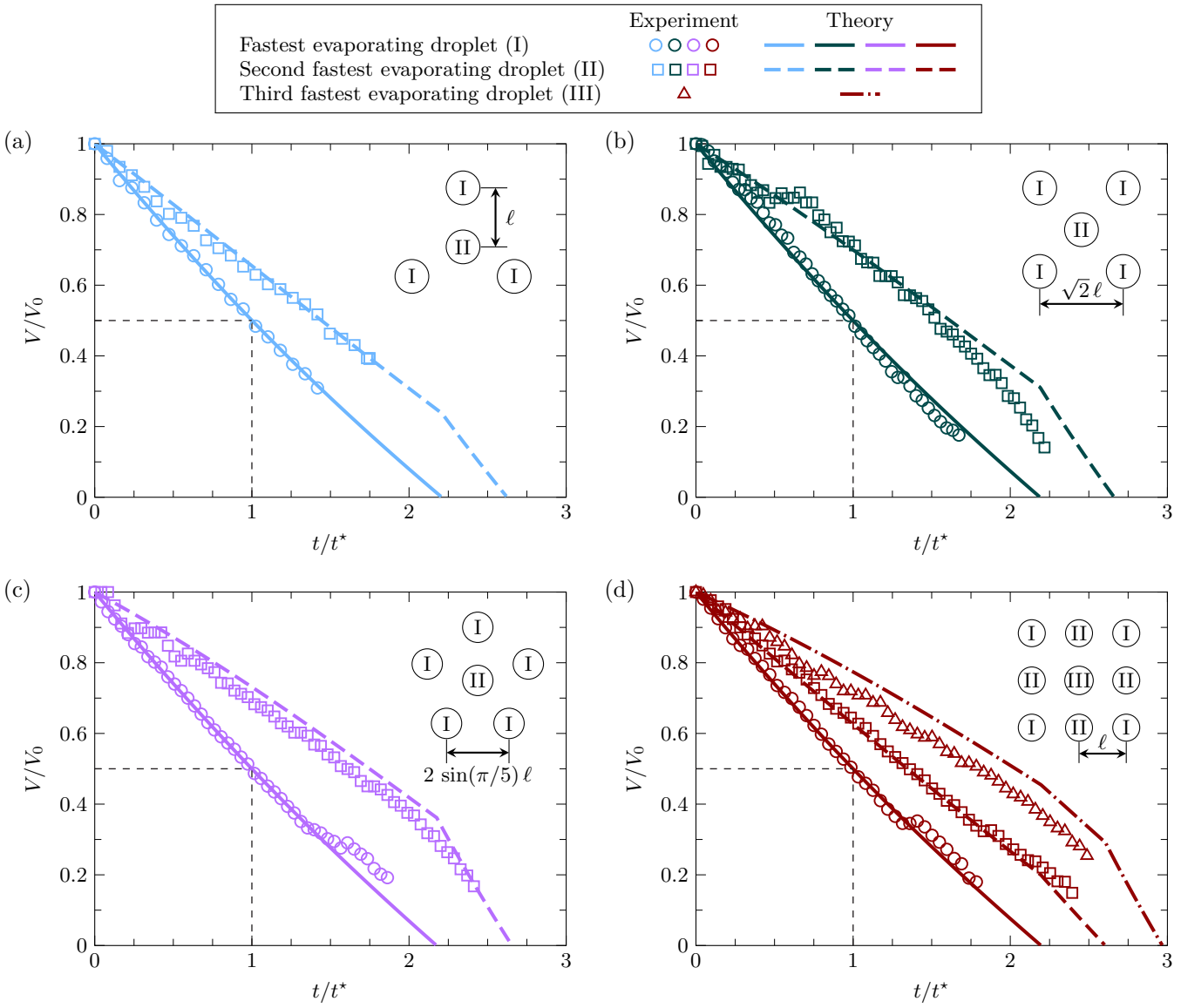

FIG. 3: Comparison between the results of experimental measurements (empty symbols) and theoretical calculations (solid and dashed lines) for the normalized volume V/V_0 versus normalized time $t/t^\star$. The plots represent the change in the volume of droplets with an initial contact angle of $\pi/2$ evaporating under CR mode while placed in arrays of four different configurations. The geometry of each array is depicted in the top right of each subfigure, where ℓ denotes the minimum center-to-center distance between droplet pairs.

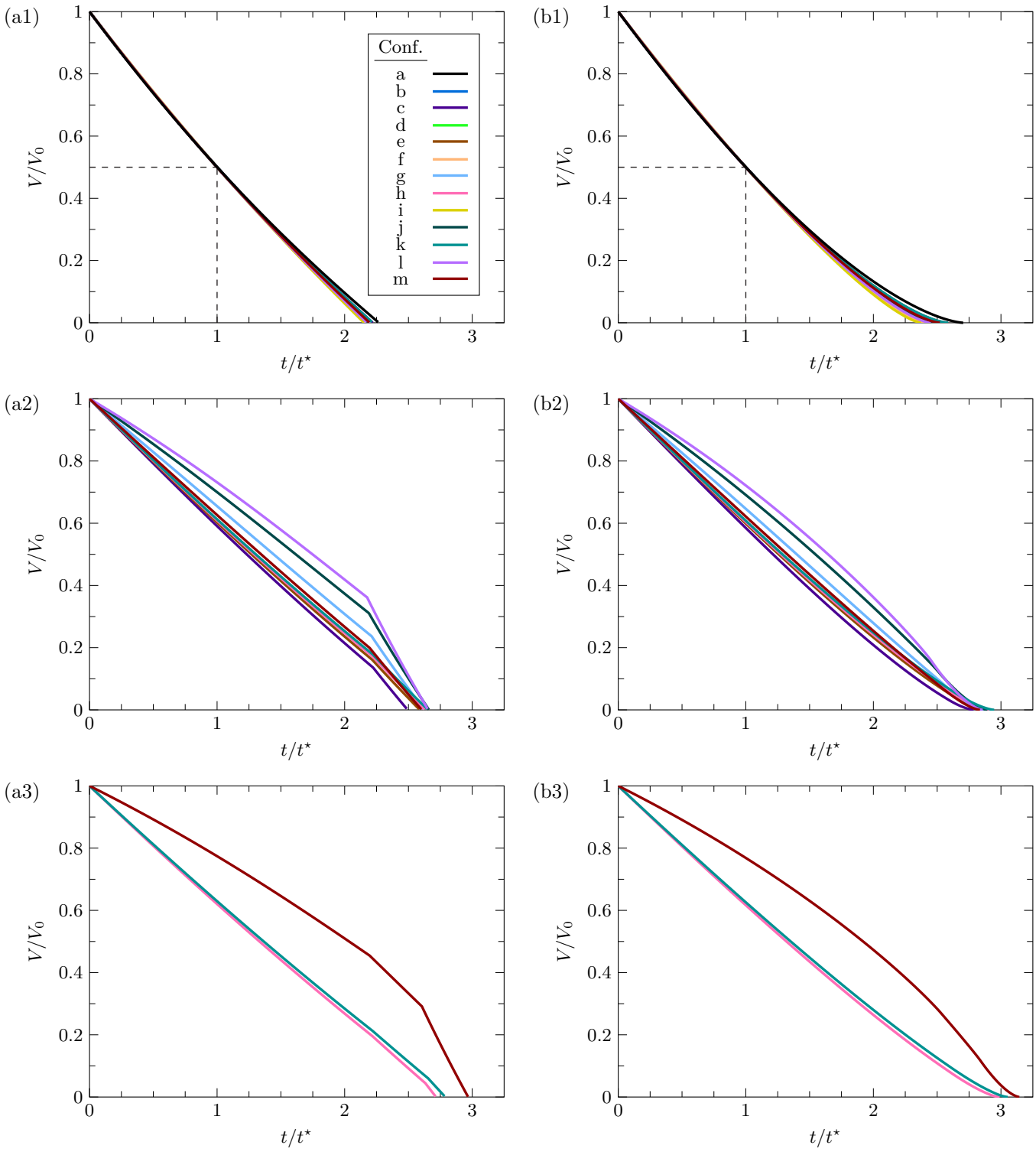

FIG. 4: Theoretically calculated plots of normalized volume V/V_0 versus normalized time $t/t^\star$ for droplets with an initial contact angle of $\pi/2$ evaporating under CR (left subfigures) and CA (right subfigures) modes while placed in arrays of different configurations. Subfigures in the first, second, and third rows show the plots for droplets of type I, II, and III, respectively. Also, configurations listed in the legend correspond to those illustrated in Fig. 7, with the exception of configuration a, which is representative of a single isolated droplet.

$\sigma = 72.75\,\mathrm{mN/m}$ were placed into an acrylic box ($W = 722\,\mathrm{mm} \times H = 510\,\mathrm{mm} \times D = 473\,\mathrm{mm}$) to prevent air currents

influencing the evaporation. Selectively hydrophobised soda-lime glass substrates with a thickness of 0.982 mm were prepared for each pattern (i.e., configurations g, j, l, and m in Fig. 7) to pin the contact line of each droplet with a base radius of $R = 0.97 \pm 0.07$ mm for approximately 80% of the drying time. The initial contact angle of the droplets was $\theta_0 \approx \pi/2$, with Bo ≈ 0.13. The relative humidity and temperature were recorded at the beginning and end of each experiment. A topdown CCD camera with a fixed $\times 0.3$ lens was focused on the image plane using a linear translation stage. The camera then recorded the evolution of the distorted pattern directly beneath the substrate as the droplets evaporated. The raw images from the camera showing the decreasing magnification as time proceeds, for each of the four droplet patterns, are presented in Fig. 2. An in-house MATLAB (MathWorks, USA) script for circle detection was used to determine the median diameter of the imaged dots within a circular region of interest, centered on the apex of each droplet, for every frame (time t). The magnification was then calculated from the ratio of this diameter to the diameter measured when the liquid had completely evaporated. Finally, the magnification was converted to a volume using the pattern distortion technique.

III. RESULTS AND DISCUSSION

We begin by assessing the agreement between the prediction of our theoretical model with the results of experimental measurements for the change in the volume of initially hemispherical droplets arranged as depicted in Fig. 2. The data obtained from both methods are presented in Fig. 3 in the form of normalized volume V/V_0 versus normalized time $t/t^\star$, where V_0 represents the value of V at $t = 0$ and $t^\star$ denotes the time taken for the fastest evaporating droplets of each array to reach half of their initial volume. For these drops, it follows that $V = V_0/2$ at $t = t^\star$ (see also the dashed lines in Fig. 3). While not unique, $t^\star$ was found to be a convenient, yet meaningful, time scale for normalizing t. In each configuration considered in Fig. 3 (and also in the following figures and table), droplets with interchangeable positions are grouped together and labeled type I, II, and III according to their order of disappearance (see the inset drawings). For experiments, the normalized volumes represent mean values over droplets of the same type, and $t^\star$ was calculated based on average V/V_0 across type I droplets. It is important to note that droplets were excluded from the averages after their contact radius was no longer pinned and the averaging was stopped after all droplets in each category have depinned, which occurred late in the drying process. Lastly, for visual clarity, every tenth point of the experimental data is plotted.

Comparing the plots of Fig. 3, we see that, overall, the experimental data validates the results of the theoretical model. The agreement level is the highest for the fastest evaporating (type I) droplets, followed by type II droplets, and, finally, by the type III drop in the 3×3 (square) array. This trend is consistent with the accuracy of the theoretical calculations, which tend to be higher for less confined droplets within each array. The observed close agreement between theory and experiment is particularly notable given the compactness of the droplet arrays. Remember that the inter-droplet distance between closest neighbors was only three times the contact radius of the droplets, i.e., $\ell = 3R$ where $\ell = 2R$ corresponds to touching drops. As noted earlier, the approximation error of Eq. (1) is generally reduced with a decrease in the contact angle of the droplets and an increase in the spacing among them. Hence, it is reasonable to expect more favorable agreements than what we have witnessed here for cases where the droplets' contact angle is less than $\pi/2$ and/or when $\ell/R > 3$. The agreements are also expected to improve when the droplets maintain their contact angle while evaporating (CA mode). In this situation, droplet-to-droplet separation widens over time resulting in progressively more accurate theoretical predictions of the evaporation rates.

Upon a closer inspection of Fig. 3, we also detect certain patterns in the drying dynamics of the droplets. Specifically, we see that, across all four arrangements, type I drops completely evaporate around $t/t^\star = 2.2$, and their V/V_0 versus $t/t^\star$ graphs behave very similarly. An analogous trend (with larger variations) is observed for type II drops, where the drying times are roughly $t/t^\star = 2.6$. Of course, a logical question that deserves attention is: how dependent are these trends on our choices of droplet arrangements, initial contact angle, and mode of evaporation? To resolve this question, we broadened our theoretical simulations in three ways by considering (i) eight more droplet configurations, (ii) two more initial contact angles ($\pi/3$ and $2\pi/3$), and (iii) evaporation under the CA mode. Figures 4, 5, and 6 show the outcomes of our additional calculations. To avoid the appearance of similar-looking figures and redundant descriptions, Figs. 5 and 6 (for, respectively, the initial contact angles of $\pi/3$ and $2\pi/3$) are presented in the appendix. Included there are also Fig. 7 that illustrates all the droplet arrangements treated theoretically and Table 1 which lists dimensionless values of $t^\star$ corresponding to the plots in Figs. 4, 5, and 6.

Inspecting the results of the extended calculations, we learn that the patterns inferred from the plots of Fig. 3 are rather general and not significantly sensitive to the arrangement of the droplets, their initial contact angle, and mode of evaporation. For both CR and CA modes, we see that the graphs corresponding to type I droplets (including those for an isolated droplet shown in black) nearly collapse into a single master curve (see subfigures a1 and b1 of Figs. 4, 5, and 6). The collapse of data is not perfect for type II droplets, while $t/t^\star$ at $V = 0$ still falling within a narrow range for all configurations (see subfigures a2 and b2 of Figs. 4, 5, and 6). Among the twelve arrangements considered,

only three (see subfigures h, k, and m of Fig. 7) have type III drops. Subfigures a3 and b3 of Figs. 4, 5, and 6 show that the curves for configurations h and k closely overlap. The plots for configuration m, however, tend to follow more curved paths, deviating from the linear trends of the overlapping plots. Despite the deviations, the ending $t/t^\star$ for all three drops (under either evaporation mode) are again fairly close to (i.e., within 10% of) each other. A couple of other noteworthy observations from Figs. 4, 5, and 6 are: (i) for the same droplet type and arrangement, $t/t^\star$ at the point of complete drying is slightly greater for evaporation under CA than CR mode and (ii) for the range of values tested here, small initial contact angles seem to marginally favor better data collapse. Lastly, Table 1 indicates that, for the same droplet arrangement and initial contact angle, $t^\star$ values corresponding to CR and CA modes differ by less than a few percentage points.

IV. CONCLUSION

We conducted theoretical calculations and experiments investigating the drying dynamics of arrays of closely-spaced droplets on a planar substrate. We found excellent agreement between the theory and experiment for four distinct configurations. Our theoretical analysis revealed similarities in the drying dynamics of type I and II droplets in all twelve arrangements illustrated in Fig. 7: for a contact angle of $\pi/2$, we found that the normalized evaporation time varied between $t/t^\star = 2.4 - 2.6$ for type I droplets and between $t/t^\star = 2.8 - 2.95$ for type II droplets. In particular, we found that $V(t)$ for type I droplets in all the geometries considered approximates that of an isolated droplet, with increasing deviation as the droplet nears its lifetime. We found similar trends for initial contact angles of $\theta_0 = \pi/6$ and $\theta_0 = \pi/3$ as well. These ideas should be applicable to other problems of diffusively dominated dynamics that involve interacting discrete objects.

[1] R. G. Larson, Transport and deposition patterns in drying sessile droplets, AIChE J. **60**, 1538 (2014).
[2] A. J. Mathijssen, M. Lisicki, V. N. Prakash, and E. J. L. Mossige, Culinary fluid mechanics and other currents in food science, arXiv: 2201.12128 (2022).
[3] S. K. Wilson and H.-M. D'Ambrosio, Evaporation of sessile droplets, Annu. Rev. Fluid Mech. **55**, 481 (2023).
[4] H. Masoud, P. D. Howell, and H. A. Stone, Evaporation of multiple droplets, J. Fluid Mech. **927**, R4 (2021).
[5] D. J. Fairhurst, Predicting evaporation rates of droplet arrays, J. Fluid Mech. **934**, F1 (2022).
[6] V. I. Fabrikant, On the potential flow through membranes, Z. Angew. Math. Mech. **36**, 616 (1985).
[7] A. W. Wray, B. R. Duffy, and S. K. Wilson, Competitive evaporation of multiple sessile droplets, J. Fluid Mech. **884**, A45 (2020).
[8] N. N. Lebedev, *Special Functions and Their Applications* (Prentice-Hall, INC., Englewood Cliffs, NJ, 1965).
[9] Y. O. Popov, Evaporative deposition patterns: spatial dimensions of the deposit, Phys. Rev. E **71**, 036313 (2005).
[10] A. M. J. Edwards, J. Cater, J. J. Kilbride, P. Le Minter, C. V. Brown, D. J. Fairhurst, and F. F. Ouali, Interferometric measurement of co-operative evaporation in 2D droplet arrays, Appl. Phys. Lett. **119**, 151601 (2021).
[11] M. L. Timm, A. Jarrahi Darban, E. Dehdashti, and H. Masoud, Evaporation of a sessile droplet on a slope, Sci. Rep. **9**, 19803 (2019).
[12] J. J. Kilbride, F. F. Ouali, and D. J. Fairhurst, In preparation, (2022).

APPENDIX

The following figures and table were excluded from the main text to avoid cluttering and to facilitate the flow of information.

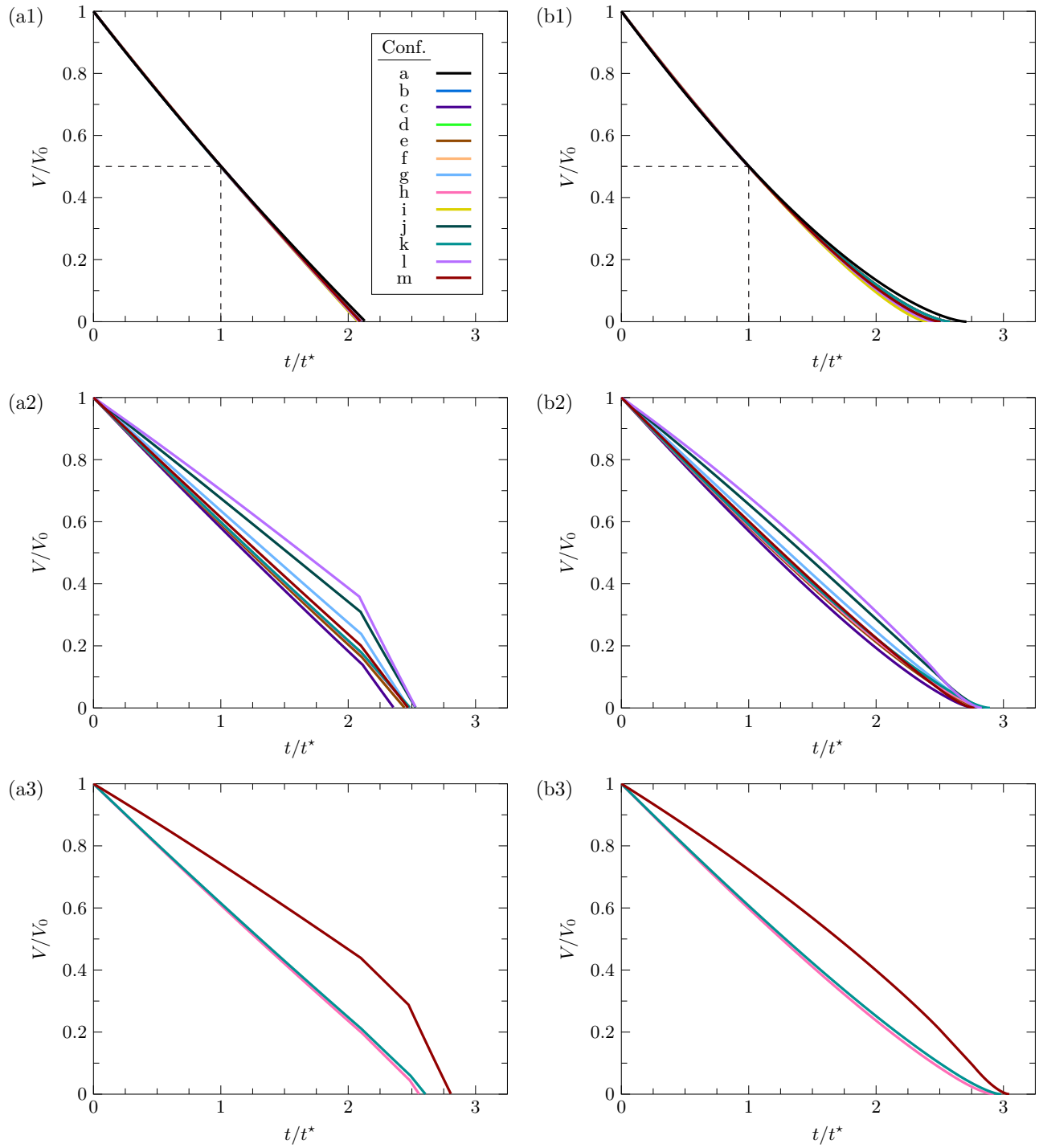

FIG. 5: Theoretically calculated plots of normalized volume V/V_0 versus normalized time $t/t^\star$ for droplets with an initial contact angle of $\pi/3$ evaporating under CR (left subfigures) and CA (right subfigures) modes while placed in arrays of different configurations. Subfigures in the first, second, and third rows show the plots for droplets of type I, II, and III, respectively. Also, configurations listed in the legend correspond to those illustrated in Fig. 7, with the exception of configuration a, which is representative of a single isolated droplet.

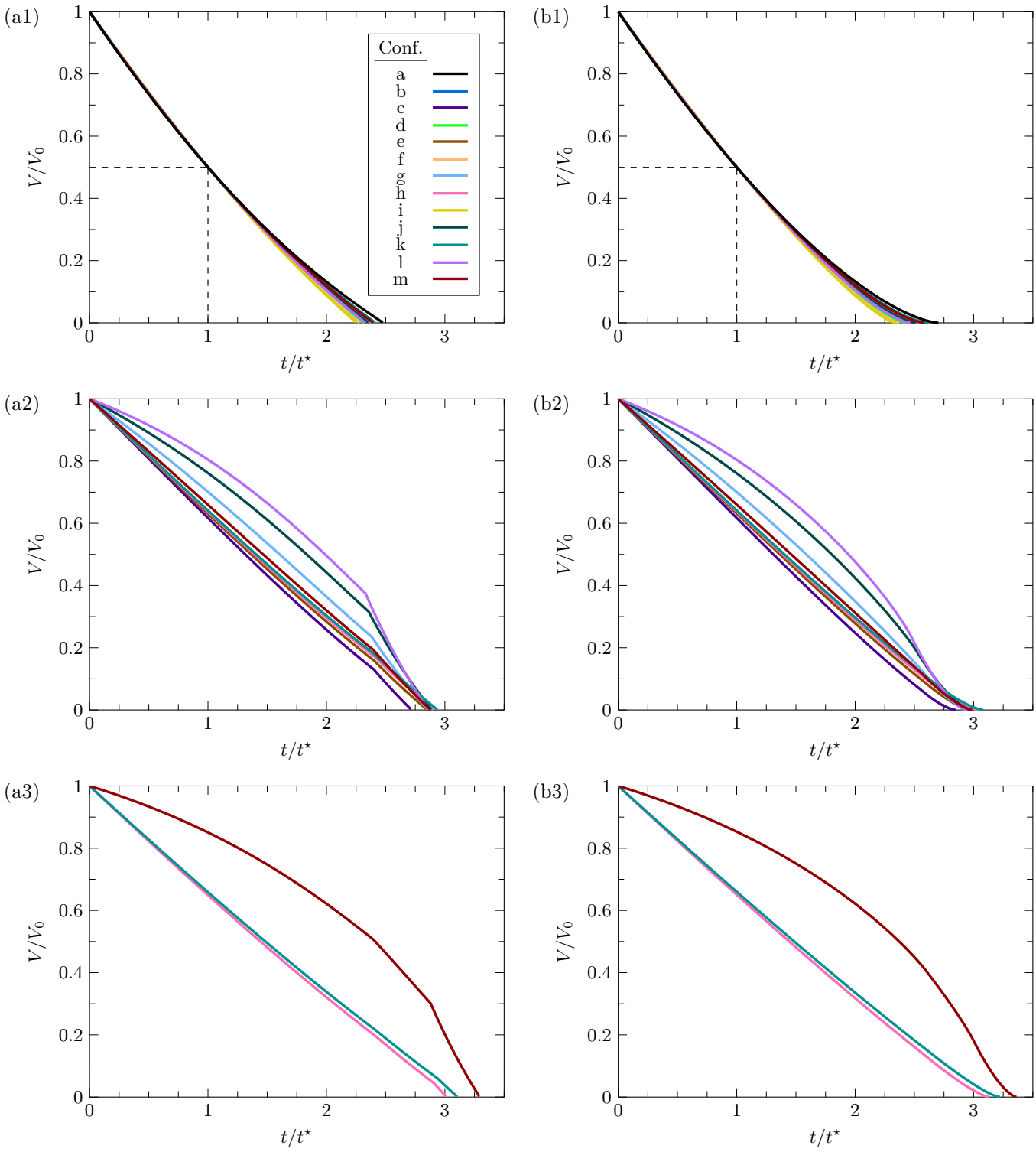

FIG. 6: Theoretically calculated plots of normalized volume V/V_0 versus normalized time $t/t^\star$ for droplets with an initial contact angle of $2\pi/3$ evaporating under CR (left subfigures) and CA (right subfigures) modes while placed in arrays of different configurations. Subfigures in the first, second, and third rows show the plots for droplets of type I, II, and III, respectively. Also, configurations listed in the legend correspond to those illustrated in Fig. 7, with the exception of configuration a, which is representative of a single isolated droplet.

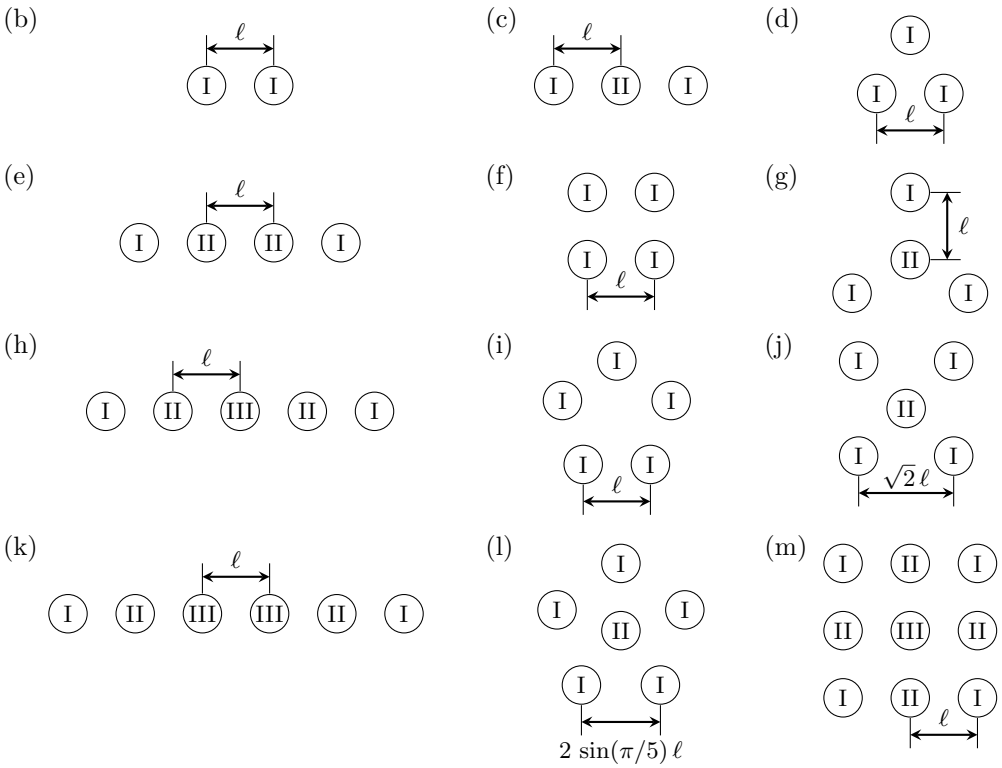

FIG. 7: Droplet arrangements considered in the theoretical calculations presented in Figs. 4, 5, and 6. In each configuration, droplets with the same rate of evaporation are grouped together and labeled I, II, or III. Also, ℓ denotes the minimum center-to-center distance between droplet pairs.

TABLE 1: Dimensionless $t^\star$ corresponding to the plots in Figs. 4, 5, and 6. The reported values are made dimensionless by $\rho R^2/\mathcal{D}\,(c_s - c_\infty)$, where R and $\mathcal{D}$ are the contact radius of the droplets and the diffusion coefficient of water vapor, respectively.

	Evaporation mode, Initial contact angle θ_0					
Configuration	CR, $\pi/3$	CR, $\pi/2$	CR, $2\pi/3$	CA, $\pi/3$	CA, $\pi/2$	CA, $2\pi/3$
a	0.105	0.183	0.345	0.110	0.185	0.342
b	0.132	0.238	0.474	0.137	0.238	0.469
c	0.141	0.255	0.513	0.146	0.257	0.508
d	0.159	0.292	0.603	0.163	0.292	0.596
e	0.147	0.267	0.539	0.152	0.268	0.533
f	0.178	0.330	0.699	0.182	0.330	0.691
g	0.156	0.284	0.581	0.161	0.286	0.576
h	0.151	0.275	0.557	0.157	0.277	0.552
i	0.192	0.359	0.773	0.196	0.359	0.764
j	0.174	0.321	0.667	0.179	0.322	0.661
k	0.155	0.281	0.571	0.160	0.283	0.566
l	0.195	0.363	0.766	0.200	0.364	0.759
m	0.211	0.393	0.822	0.218	0.395	0.815